

RESEARCH ARTICLE

10.1002/2017JD028155

Key Points:

- Ensemble sensitivity analysis was conducted on a heavy rainfall case featured with stage-dependent rainfall forecast skills
- The stage-dependent rainfall forecast skills were mainly caused by forecast uncertainties in the location of the low-level jet (LLJ)
- The uncertainty of LLJ location was related to juxtapositions between direction of the low-level vortex movement and LLJ orientation

Correspondence to:

Z. Meng,
zymeng@pku.edu.cn

Citation:

Zhang, M., & Meng, Z. (2018). Impact of synoptic-scale factors on rainfall forecast in different stages of a persistent heavy rainfall event in south China. *Journal of Geophysical Research: Atmospheres*, 123, 3574–3593. <https://doi.org/10.1002/2017JD028155>

Received 3 DEC 2017

Accepted 15 MAR 2018

Accepted article online 23 MAR 2018

Published online 13 APR 2018

Impact of Synoptic-Scale Factors on Rainfall Forecast in Different Stages of a Persistent Heavy Rainfall Event in South China

Murong Zhang¹  and Zhiyong Meng¹ 

¹Laboratory for Climate and Ocean-Atmosphere Studies, Department of Atmospheric and Oceanic Sciences, School of Physics, Peking University, Beijing, China

Abstract This study investigates the stage-dependent rainfall forecast skills and the associated synoptic-scale features in a persistent heavy rainfall event in south China, Guangdong Province, during 29–31 March 2014, using operational global ensemble forecasts from the European Centre for Medium-Range Weather Forecasts. This persistent rainfall was divided into two stages with a better precipitation forecast skill in Stage 2 (S2) than Stage 1 (S1) although S2 had a longer lead time. Using ensemble-based sensitivity analysis, key synoptic-scale factors that affected the rainfall were diagnosed by correlating the accumulated precipitation of each stage to atmospheric state variables in the middle of respective stage. The precipitation in both stages was found to be significantly correlated with midlevel trough, low-level vortex, and particularly the low-level jet on the southeast flank of the vortex and its associated moisture transport. The rainfall forecast skill was mainly determined by the forecast accuracy in the location of the low-level jet, which was possibly related to the different juxtapositions between the direction of the movement of the low-level vortex and the orientation of the low-level jet. The uncertainty in rainfall forecast in S1 was mainly from the location uncertainty of the low-level jet, while the uncertainty in rainfall forecast in S2 was mainly from the width uncertainty of the low-level jet with the relatively accurate location of the low-level jet.

1. Introduction

Heavy rainfall frequently occurs over south China during warm season under the influence of Mei-Yu fronts (Chen, 1983), low-level vortices that develop in southwestern China (Tao & Ding, 1981), low-level jets (e.g., Chen et al., 2014; Kuo & Chen, 1990), land–sea breezes (e.g., Chen et al., 2015, 2017), and cold pools produced by previous precipitation (Wang, Luo, & Jou, 2014; Wu & Luo, 2016). Although impacts of various synoptic-scale weather systems on heavy rainfall over south China have been recognized in the literature, their relative importance and the uncertainties of the key synoptic-scale factors in numerical models that influence the quantitative forecast skills of heavy rainfall event in south China have not been investigated.

Key synoptic-scale factors of extreme rainfall events have been examined in other regions using ensemble-based sensitivity analysis (ESA; Hakim & Torn, 2008) with the accumulated precipitation serving as a forecast metric. For example, Schumacher (2011) examined the factors contributing and inhibiting the development of a heavy rainfall in warm season in the United States based on the ensemble forecast from the European Centre for Medium-Range Weather Forecasts (ECMWF) Ensemble Prediction System (EPS). Lynch and Schumacher (2014) found that a stronger low-level cyclone over central U.S. was associated with less precipitation over Kentucky and Tennessee in the extreme rainfall event in May 2010. Yu and Meng (2016) disclosed the key synoptic factors of an extremely heavy rainfall in north China using ESA based on a grand ensemble forecast from National Centers for Environmental Prediction, ECMWF, and China Meteorological Administration. One objective of this current study is to reveal the key synoptic-scale factors of a heavy rainfall event in warm season of south China by applying ESA to ECMWF ensemble forecast.

Warm-season heavy rainfall in south China can sometimes sustain for tens of hours (e.g., Davis & Lee, 2012; Li et al., 1997; Luo et al., 2017; Zhang et al., 2011). Distinct rainfall characteristics and dynamical mechanisms of precipitation have been noticed in different rainfall stages of persistent rainfall events (e.g., Gao et al., 2009; Wang et al., 2014a, 2014b). Notably, in some cases in south China, the forecast skill of precipitation varies from stage to stage during persistent rainfall process (e.g., Gao et al., 2009). However, the studies on different forecast skills over different stages in persistent heavy rainfall in

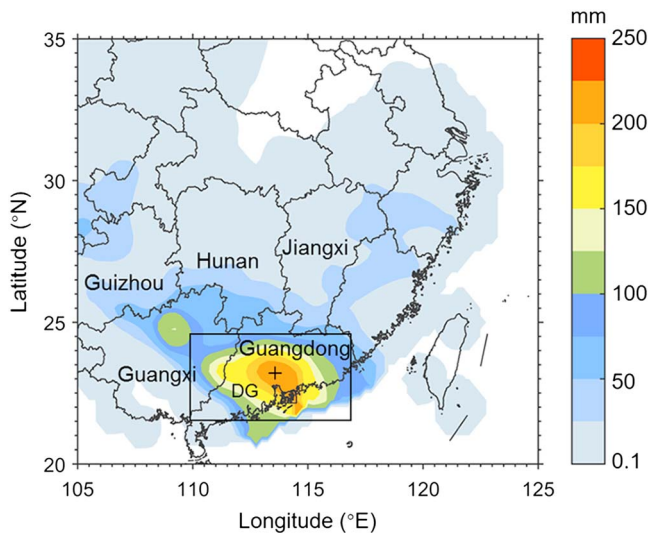


Figure 1. Three-day accumulated precipitation (shading in mm) between 0000 UTC 29 March and 0000 UTC 1 April 2014 with the black box indicating the location of area used for averaging precipitation (the control area). The location of Dongguan Station (DG) is marked as the black cross and the provinces mentioned in text are given in the map.

50.88 million CNY (China Yuan), seven deaths (available online at <http://news.cntv.cn/2014/04/01/ARTI1396335268149564.shtml> on 15 February 2017), and a large number of flight delays (Feng et al., 2014). During this heavy rainfall event, there were two distinct rainfall amount peaks (Figure 3; more details later in section 3) indicating different rainfall stages. Considering the significant rainfall underestimation around the two distinct rainfall peaks from 0000 UTC 30 March to 0000 UTC 31 March 2014 compared with other periods and their apparently different forecast errors between each other, the first rainfall stage was defined as from 0000 to 1200 UTC 30 March and the second stage from 1200 UTC 30 March to 0000 UTC 31 March (hereafter S1 and S2). The operational forecasts showed a better precipitation forecast skill in terms of both amount and distribution in S2 than S1 even though S2 had a longer lead time, suggesting the stage-dependent rainfall forecast skills.

The innovation of the present study mainly lies in three aspects: (1) identifying key synoptic-scale factors and their associated uncertainties in numerical models for a warm-season heavy rainfall event in south China, (2) disclosing reasons behind stage-dependent feature of rainfall forecast skills, and (3) for the first time applying ESA method to analyze its applicability to the torrential rain in south China. Section 2 describes the data and methods used in the study. Section 3 provides an overview of the event. In section 4, results of forecast verification, ensemble-based sensitivity analysis, and reasons for different forecast skills of the two stages at synoptic scale are presented in turn. Summary and conclusions are given in section 5.

2. Data and Methods

Hourly rain gauge data provided by China Meteorological Administration with an average site spacing of ~ 10 km were interpolated to a 0.25° by 0.25° grid using a Cressman interpolation method (Cressman, 1959) so that it can be compared with global model forecast conveniently. The ERA-Interim (the ECMWF Interim Reanalysis dataset; Dee et al., 2011) with a horizontal grid spacing of 0.5° (interpolated from the original horizontal grid spacing of ~ 80 km) at a 6 hr interval was used for synoptic environmental analyses, similar to Lynch and Schumacher (2014). We chose 0.5° as the horizontal grid spacing for ERA-Interim in order to make a reasonable comparison with ECMWF ensemble forecast, since the original horizontal grid spacing of the ECMWF ensemble forecast is ~ 32 km and 0.5° is between 32 and 80 km.

The ECMWF global ensemble forecast was used to examine the different key factors of the two rainfall stages. The EPS of ECMWF was chosen because it has a large ensemble size and a well-tuned ensemble spread (Park et al., 2008). The ECMWF EPS contains 50 ensemble members with a truncation of T639 (about 32-km grid

south China are still limited. A better understanding on the stage-dependent forecast skills of heavy rainfall is necessary to provide better references for more detailed precipitation forecasting. Another objective of the present study is to investigate the reasons for distinctive forecast skills over different stages in a persistent warm-season heavy rainfall in south China by comparing the key factors and their uncertainties in different stages.

The heavy rainfall case examined in this paper occurred during 29–31 March 2014 in Guangdong Province (denoted in Figure 1, hereafter Guangdong for short) in south China. As shown in the 72 hr accumulated precipitation (Figure 1), a large amount of precipitation was observed in the Pearl River Delta region, southeast of Guangdong, with the maximum value of 264.8 mm located at Dongguan (denoted by the cross mark in Figure 1). This rainfall process was characterized by long period and great intensity and signified the beginning of the rainy season in 2014 in Guangdong according to the operational definition, which was much earlier than usual (Wang & Cheng, 2014). The heavy rainfall associated with strong wind and hail led to destructive flooding and damage of infrastructure in megacities such as Guangzhou and Shenzhen (locations given in Figure 2a), resulting in direct property damage of

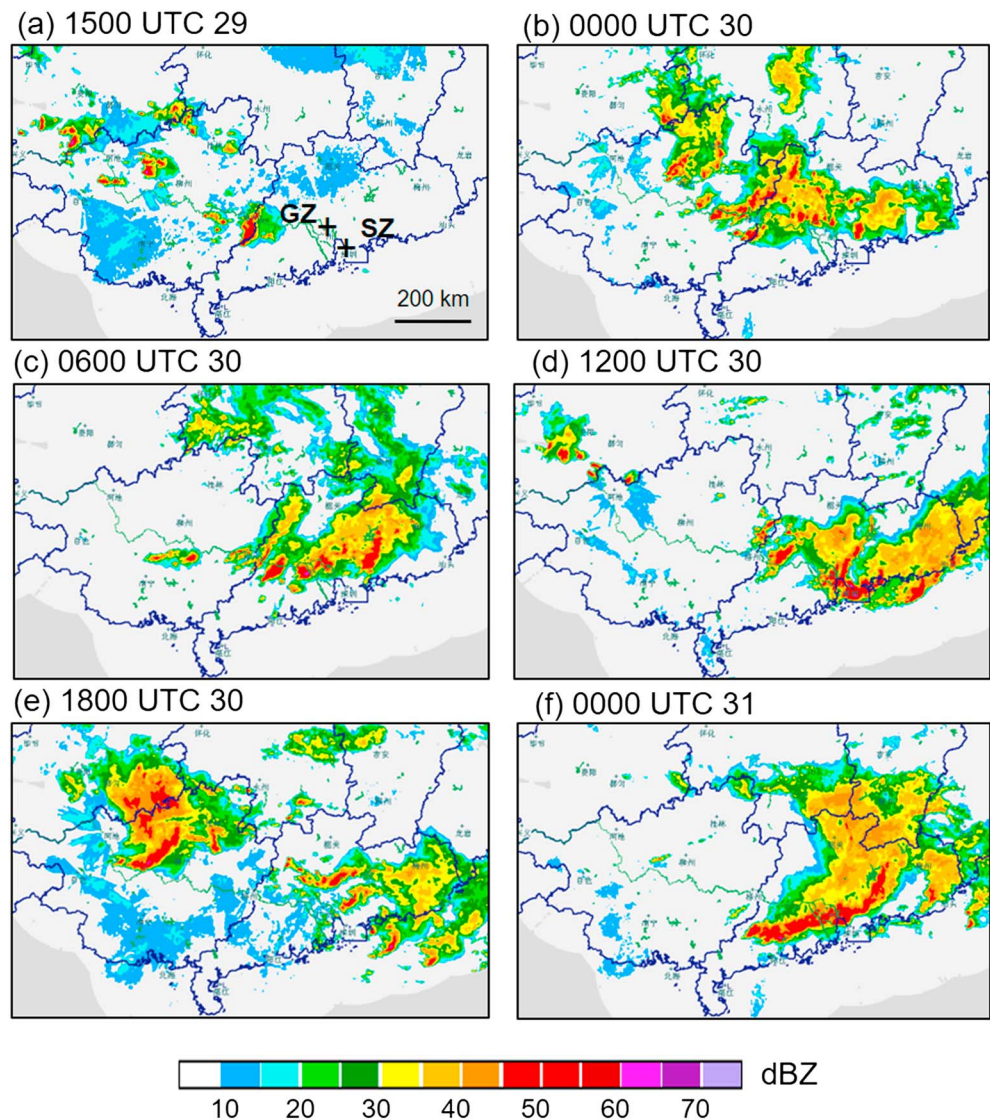


Figure 2. Composite reflectivity imagery (shaded in dBZ) of (a) 1500 UTC 29 March, (b) 0000 UTC 30 March, (c) 0600 UTC 30 March, (d) 1200 UTC 30 March, (e) 1800 UTC 30 March, and (f) 0000 UTC 31 March 2014. Locations of Guangzhou (GZ) and Shenzhen (SZ) are given in (a).

spacing) through a 240-hr forecast period (details are available online at <https://www.ecmwf.int/sites/default/files/elibrary/2012/14557-ecmwf-ensemble-prediction-system.pdf>). To enlarge the sample size and obtain more robust results that are not affected by different forecast lead times, we collected three ensembles that were valid at the same time but with different initial times of 0000 UTC 29 March, 1200 UTC 29 March, and 0000 UTC 30 March, respectively, and composed a new ensemble of 150 members (the ensemble mentioned hereafter refers to this 150-member new ensemble except for being stated otherwise). The ensemble forecast data have a horizontal grid spacing of 0.5° (except for precipitation, which has a horizontal grid spacing of 0.25°) with a 6-hr interval.

ESA was used in this study to identify the key factors for the rainfall, which measures linear relationships between a scalar forecast metric and atmospheric state variables through ensemble statistics. This method was first introduced by Hakim and Torn (2008) and has been widely used to diagnose key factors for persistent extreme rainfall events as being mentioned in section 1 (e.g., Lynch & Schumacher, 2014; Schumacher, 2011; Yu & Meng, 2016) and to understand the predictability and the dynamical processes of weather systems such as extratropical cyclones (e.g., Garcies & Homar, 2009; McMurdie & Ancell,

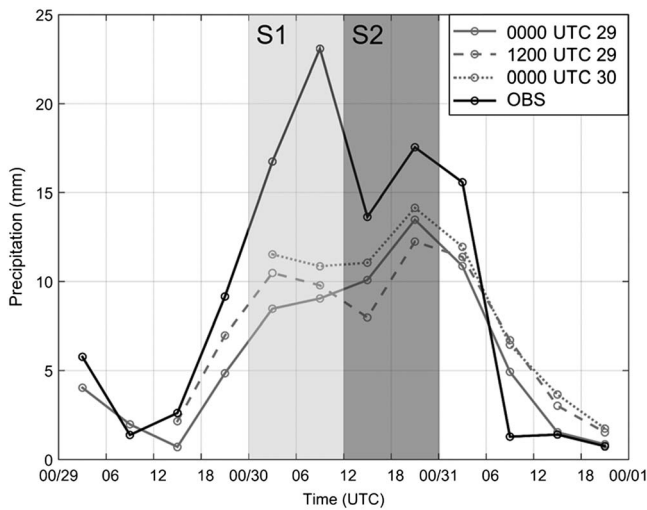


Figure 3. Evolution of area-averaged 6-hr accumulated precipitation over the black box in Figure 1 of observation and ensemble mean forecast from ECMWF. The black solid line indicates the observation, and the ensemble mean forecasts that initialized at 0000 UTC 29 March, 1200 UTC 29 March, and 0000 UTC 30 March 2014 are denoted by solid, dashed, and dotted gray lines, respectively. Time range of the two rainfall stages are shown by light (S1) and dark (S2) gray shading.

2014), mesoscale convective vortices (Hawblitzel et al., 2007), tropical cyclones (e.g., Sippel & Zhang, 2008, 2010), and extratropical transitions (Torn, 2010). Compared with other sensitivity analysis methods such as ensemble Kalman filter (Ansell, 2013), Piece-By-Piece Data Assimilation targeting method (Huang & Meng, 2014), and adjoint analysis (Le Dimet & Talagrand, 1986; Mu & Duan, 2003; Yu et al., 2017), ESA is more straightforward and easier to implement especially with the availability of TIGGE (The Observing System Research and Predictability Experiment Interactive Grand Global Ensemble; Bougeault et al., 2010) ensemble forecast database. It can reveal the relative importance (based on the magnitude of correlations) of various influencing factors in rainfall processes and some relationships that may not be obvious to find using other analysis techniques. In the present study, the area-averaged 12-hr accumulated precipitation of both observation and forecast in the two stages was calculated as forecast metrics. Pearson correlation coefficient was used to measure the magnitude of linear relationship between 12-hr accumulated precipitation averaged over 21.5–24.5°N, 110–117°E (denoted by the black box in Figure 1, hereafter the control area) and variables of interest at each grid at different forecast times. At a certain grid point, the Pearson correlation coefficient was calculated as follows:

$$r = \frac{\sum_{i=1}^n (X_i - \bar{X})(P_i - \bar{P})}{\sqrt{\sum_{i=1}^n (X_i - \bar{X})^2 \sum_{i=1}^n (P_i - \bar{P})^2}} \quad (1)$$

where P is the area-averaged 12-hr accumulated precipitation, X is the atmospheric variable of interest at certain forecast time at this grid point, the overbar represents the mean of the variable, and n is the ensemble size ($n = 150$ herein). Assuming that the 150 members have equal probability, the linear relationship is statistically significant at 95% confidence level under two-tailed Student's t test when correlation coefficient is greater than 0.1602. The equitable threat score (ETS) (Wilks, 1995) was applied in this study to measure the rainfall forecast skill.

3. Case Overview

In this persistent rainfall process, widespread convective cells were initiated in Guangxi Province (its location is given in Figure 1, hereafter Guangxi for short) at 1500 UTC 29 March (Figure 2a) and propagated eastward, gradually evolving into a large MCS in Guangdong. A west–east oriented rainband formed at around 0000 UTC 30 March (Figure 2b). S2 was mainly featured with a long squall line with a strong bow structure (Figures 2e and 2f). Successive MCSs led to persistent heavy rainfall in Guangdong.

The synoptic environment of this event was examined using ERA-Interim analysis fields at 0600 and 1800 UTC 30 March, which were closest to the times of two rainfall peaks, respectively (black line in Figure 3). The 500-hPa geopotential height revealed a short trough to the northwest of Guangdong (Figure 4a), and the trough became shallower as moving eastward (Figure 4b). The axis of the subtropical high was located around 15°N (Figure 4a). A cyclonic vortex at 850 hPa was located over south China and propagated eastward with a low-level jet (defined as a wind belt with a speed of no less than 12 m/s) embedded in its southeast flank (shaded in Figures 4c and 4d). The 850-hPa synoptic circulation presented a saddle-like pattern, which is typical in premonsoon season in south China according to Wu et al. (2010). A surface low resided in western Guangxi at 0600 UTC and moved eastward with the 850-hPa vortex (Figures 4e and 4f). In the meantime, a surface convergence line stayed persistent along the coastal area of Guangdong. The evolution of total column water (Figure 5) showed sufficient moisture transport from the South China Sea (SCS). During the 3 days, total column water in most parts of Guangdong was over 40 mm. To summarize, this heavy rainfall event was under the influence of the mid-level short trough, the low-level vortex, and the low-level jet.

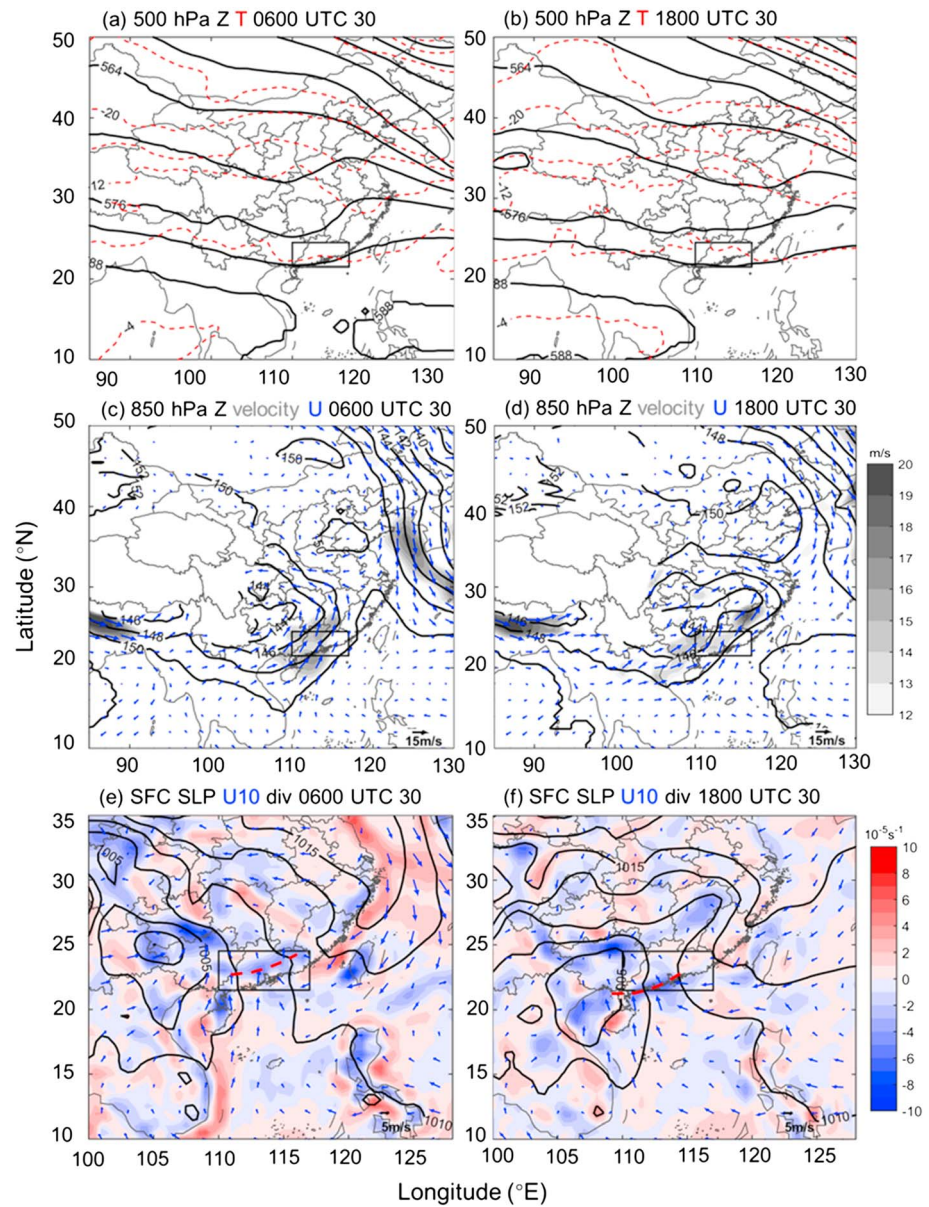


Figure 4. Synoptic environment during the heavy rainfall event. The 500-hPa geopotential height (contoured in black every 40 gpm) and 500-hPa temperature (contoured in red dash every 4°C) at (a) 0600 and (b) 1800 UTC 30 March 2014; 850-hPa geopotential height (contoured in black every 20 gpm), 850-hPa wind vector (blue vector, scale is shown at bottom right), and wind speed (shaded over 12 m/s) at (c) 0600 and (d) 1800 UTC 30 March 2014. Sea level pressure (contoured in black every 2.5 hPa), 10 m wind vector (blue vector; scale is shown at bottom right), and divergence of bottom model level (shaded, $10^{-5}/s$) at (e) 0600 and (f) 1800 UTC 30 March 2014. The red thick dashed line in (e) and (f) denotes the location of surface convergence line. The black boxes in all the panels denote the control area, the same as that in Figure 1.

4. Results

4.1. Forecast Verification

The ensemble mean of ECMWF EPS had a better rainfall forecast skill in S2 than S1. All of the three ensembles with different initial times missed the first rainfall peak (Figure 3) while having a better performance in S2. According to the ensemble mean forecast, the predicted maximum rainfall magnitude in S1 was apparently smaller and the rainfall shifted much to the northwest of the observed surface rainfall

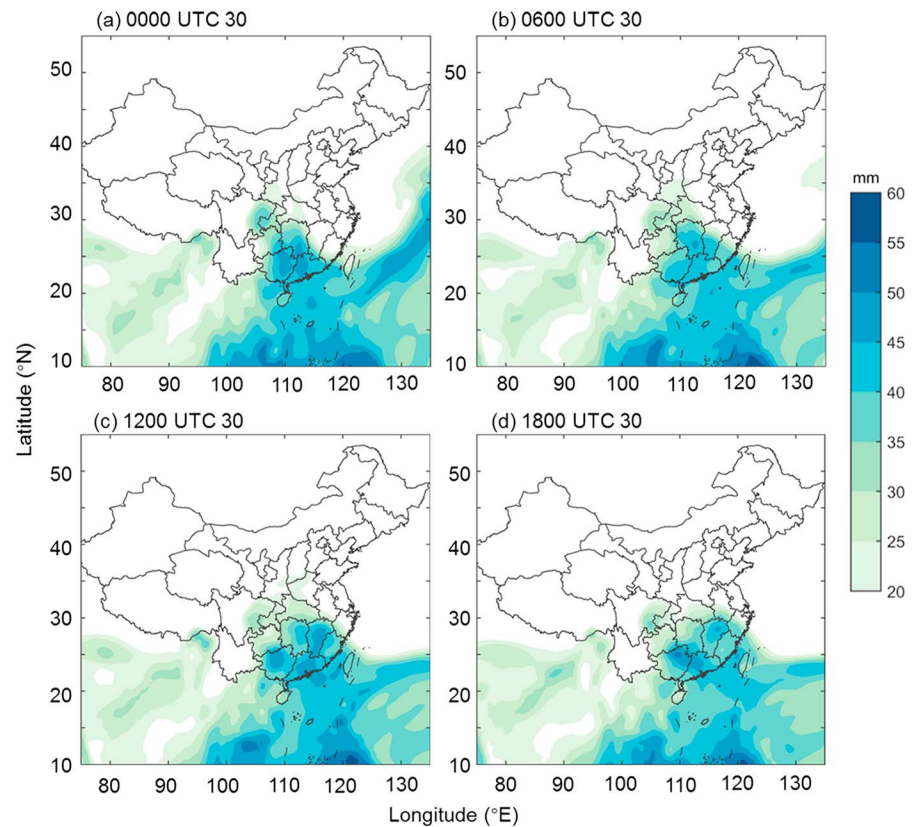


Figure 5. Total column water (mm) of ERA-Interim reanalysis at (a) 0000, (b) 0600, (c) 1200, and (d) 1800 UTC on 30 March.

center (Figures 6a and 6b), while the rainfall maxima and the rainfall distribution in S2 were quite similar to the observation (Figures 6c and 6d). To compare the rainfall forecast skills in different stages quantitatively, ETSS of individual ensemble members were examined (Figure 7). Considering the coarse resolution of global ensemble forecasts, only the ETSS for 30-mm and 40-mm thresholds were examined to reveal the different forecast skills of rainfall. The ensemble mean ETSS (green lines in Figure 7) in S1 was lower than S2 at different thresholds. Notably, most of the members underestimated the precipitation in both stages and especially in S1. The scatterplot reflects the strong positive correlation ($r > 0.6$) between 12-hr area-averaged precipitation and ETSS scores in both stages.

The ensemble forecast in the two stages was further examined by comparing ensemble members with different forecast performances. To determine members with the most and the least accurate rainfall forecast, the rainfall distribution and the precipitation amount of individual members were subjectively compared with observation, and ETSSs of individual members were also considered as objective metrics. By this way, members 97, 113, 131, and 140 were chosen as good members, while members 26, 38, 63, and 100 were chosen as bad members in S1. In S2, members 7, 122, 123, and 135 were chosen as good members, while members 15, 34, 71, and 92 were chosen as bad members (red and blue circles, respectively, in Figure 7). The rainfall distributions of some of these members in S1 and S2 are shown in Figures 8a–8d and Figures 8e–8h, respectively. Good members in S1 (Figures 8a and 8c) had a rainfall distribution quite similar to that of the observation, while the rainfall in bad members in S1 (Figures 8b and 8d) was located to the northwest of the observation with less precipitation amount. In S2, good members predicted a rainfall pattern quite similar to the observation even though some of them overestimated local maximum precipitation such as member 7 (Figures 8e and 8g); bad members predicted a widespread rainfall area to the north of Guangdong (Figures 8f and 8h).

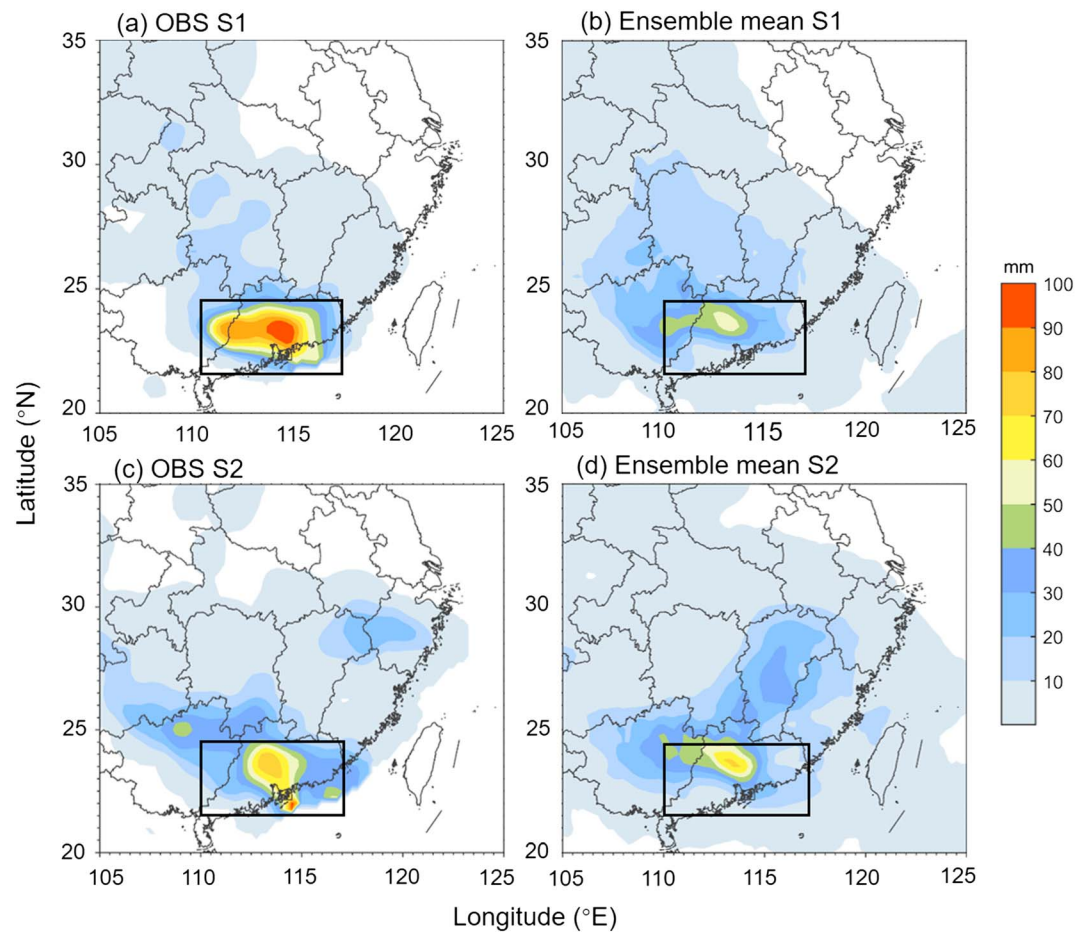


Figure 6. Precipitation distribution of observation and ensemble mean in the two stages. 12-hr accumulated precipitation of (a) observation and (b) ensemble mean in S1 are shaded; (c) and (d) are as (a) and (b) but for S2. The black boxes in all the panels denote the control area, the same as that in Figure 1.

4.2. Key Factors of the Rainfall in Different Stages

ESA was applied to examine the correlations between the accumulated rainfall averaged over the control area in different stages and atmospheric state variables at 0600 and 1800 UTC 30 March, which were at the beginning of the most intense rainfall periods (0600–1200 UTC 30 March and 1800 UTC 30 March–0000 UTC 31 March), to better reveal key factors for the heavy rainfall in respective stages. Comparisons between composite fields of good members and bad members were then performed to provide more physical insight of sensitive areas.

4.2.1. Westerly Trough and Low-Level Vortex

Analyses on the correlation coefficients between 500-hPa geopotential height and accumulated precipitation in the two stages showed that the rainfalls in both stages had a strong correlation with the midlevel short trough. The correlation between the forecast of 500-hPa geopotential height at 0600 UTC 30 March and area-averaged rainfall in S1 reflected a large negative area ($r \approx -0.4$) over southeastern Guangdong (Figure 9a). This suggests that lower height in this area, indicating a deeper short trough, was associated with more precipitation over the control area in S1. The correlation between the 500-hPa height at 1800 UTC 30 March and area-averaged rainfall in S2 showed a negative area over southeastern Guangdong (Figure 9b) with an upstream positive area to northwestern Guangdong, indicating that the strength of short trough also influenced the precipitation in S2 significantly.

Similar calculations were also performed for 850-hPa height (Figures 9c and 9d). In S1, the correlation between geopotential height on 850 hPa and precipitation was strongly negative ($r \approx -0.5$, stronger than

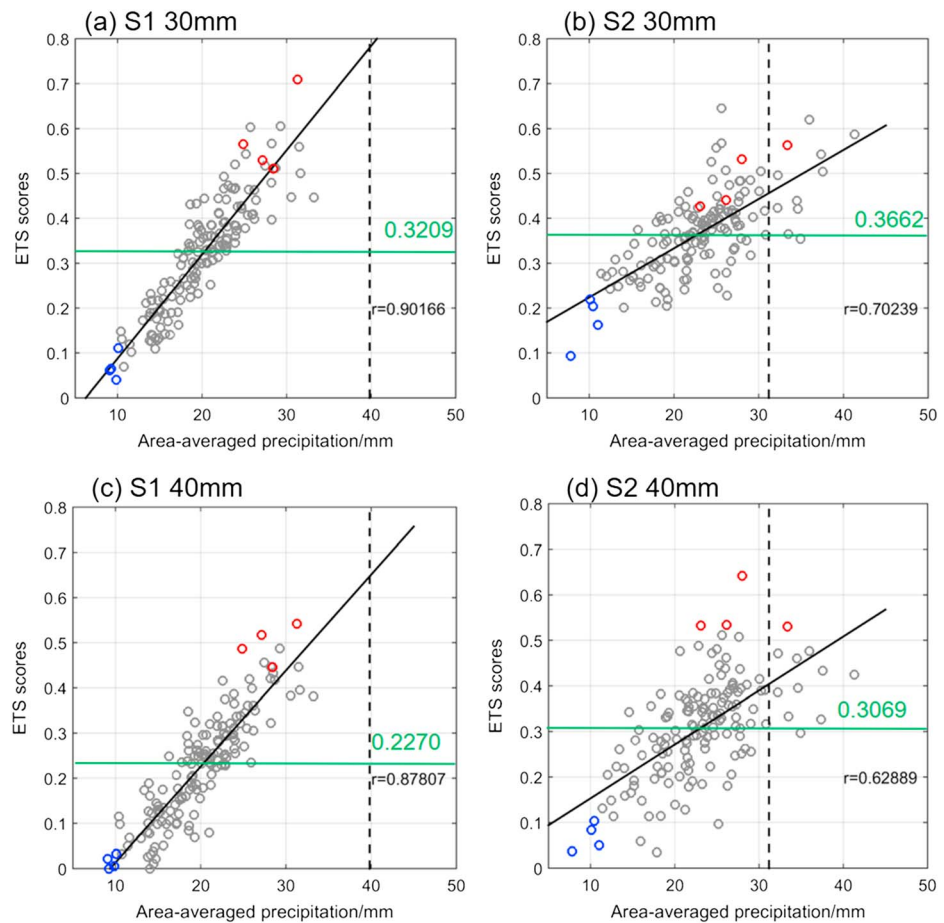


Figure 7. Area-averaged precipitation versus ETS scatterplot for the thresholds of (a, b) 30 mm and (c, d) 40 mm for the two stages. The ETs were calculated over the black box shown in Figure 1. Good (bad) members are plotted in red (blue) circles, and other members are plotted in grey circles. The dashed black line represents the observed area-averaged precipitation. The thin black line represents the best fit line. The green line indicated the value of ensemble mean ETS.

that on 500 hPa) in most Guangdong area, implying that a more southeastward low-level vortex would lead to more precipitation in S1. However, in S2 the distribution of sensitive area on 850 hPa (Figure 9d) became quite different: a couple of positive and negative areas were located near the low-level vortex. The positive area covered the center of the low-level vortex and its north boundary, while the negative area covered its south boundary. Higher geopotential height at the center and north parts of the vortex, and lower geopotential height at the south part of the vortex, was associated with more accumulated precipitation in S2. Considering that a sensitivity dipole is often associated with positional sensitivities to boundary or synoptic system placement (Bednarczyk & Ancell, 2015), the correlation pattern in S2 suggests that a weaker low-level vortex with more southeast placement was favorable for more precipitation in S2. Similar correlation patterns were also found for 700-hPa geopotential height (not shown) and sea level pressure (Figures 10a and 10b).

To further confirm the sensitivity signal obtained by ESA, comparisons on geopotential height between composite fields of good and bad members were performed at 0600 (S1) and 1800 UTC 30 March (S2), respectively. On 500 hPa (Figures 11a and 11b), good members in both stages forecasted a deeper short trough over Guangdong, while in bad members there was no noticeable short trough. These differences were highly consistent with ESA results. On 850 hPa, the precipitation in S1 and S2 were influenced by the low-level vortex in different ways. In S1, the rainfall in the control area was more associated with the position of low-level vortex. Good members forecasted a low-level vortex more to the southeast so that the geopotential height in

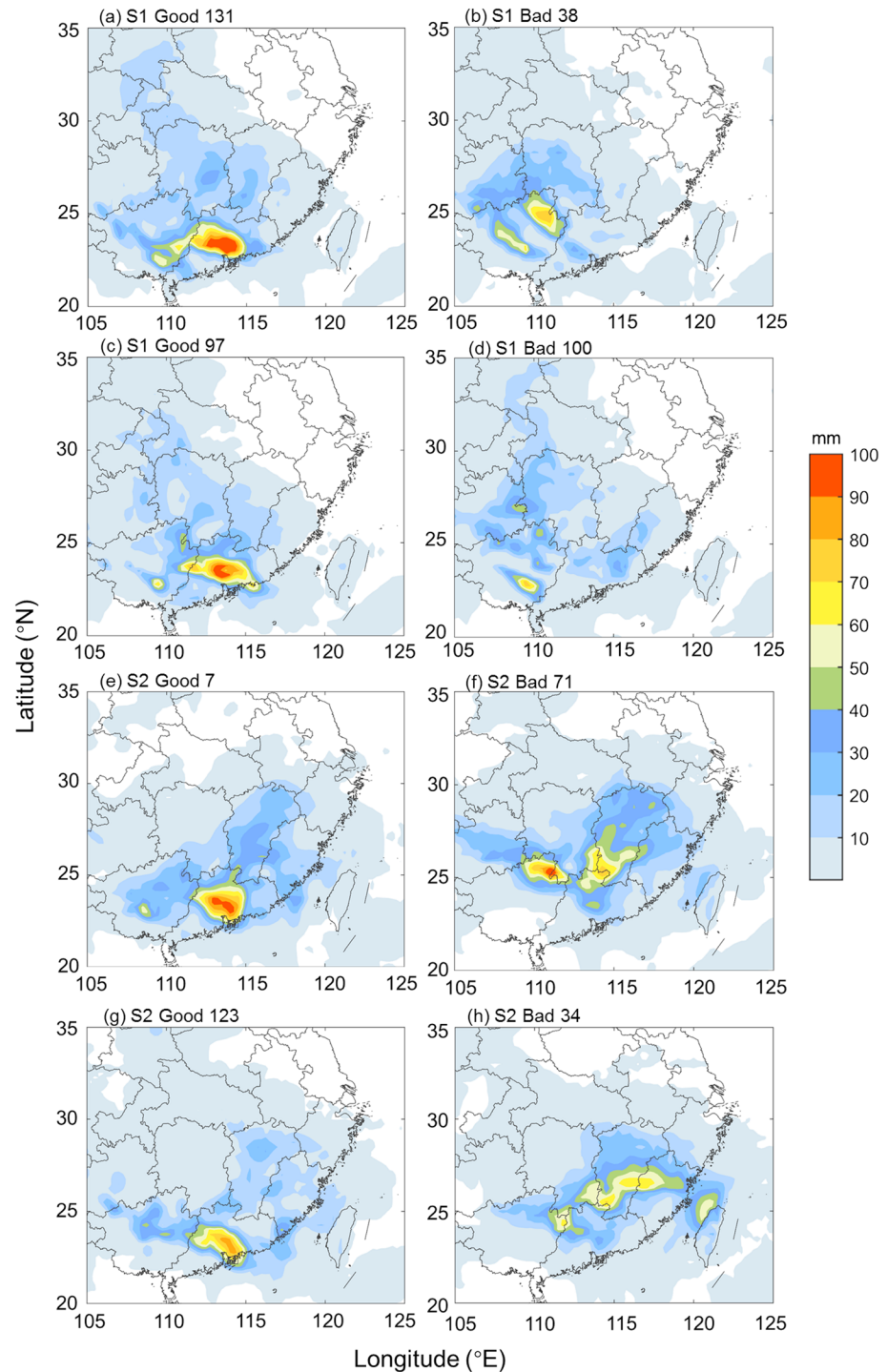


Figure 8. Rainfall distributions of some of the typical members in the two stages. The 12-hr accumulated precipitation in S1 of good members (a) 131 and (c) 97 and bad members (b) 38 and (d) 100 and the 12-hr accumulated precipitation in S2 of good members (e) 7 and (g) 123 and bad members (f) 71 and (h) 34.

the control area was lower compared with that in bad members (Figure 11c). A more-to-the-southeast low-level vortex led to a more-to-the-southeast low-level jet and eventually contributed to more rainfall in the control area. In S2, the rainfall in the control area was more associated with the strength of the low-level vortex. Good members had weaker low-level vortices (approximately 20 gpm higher in the center of the

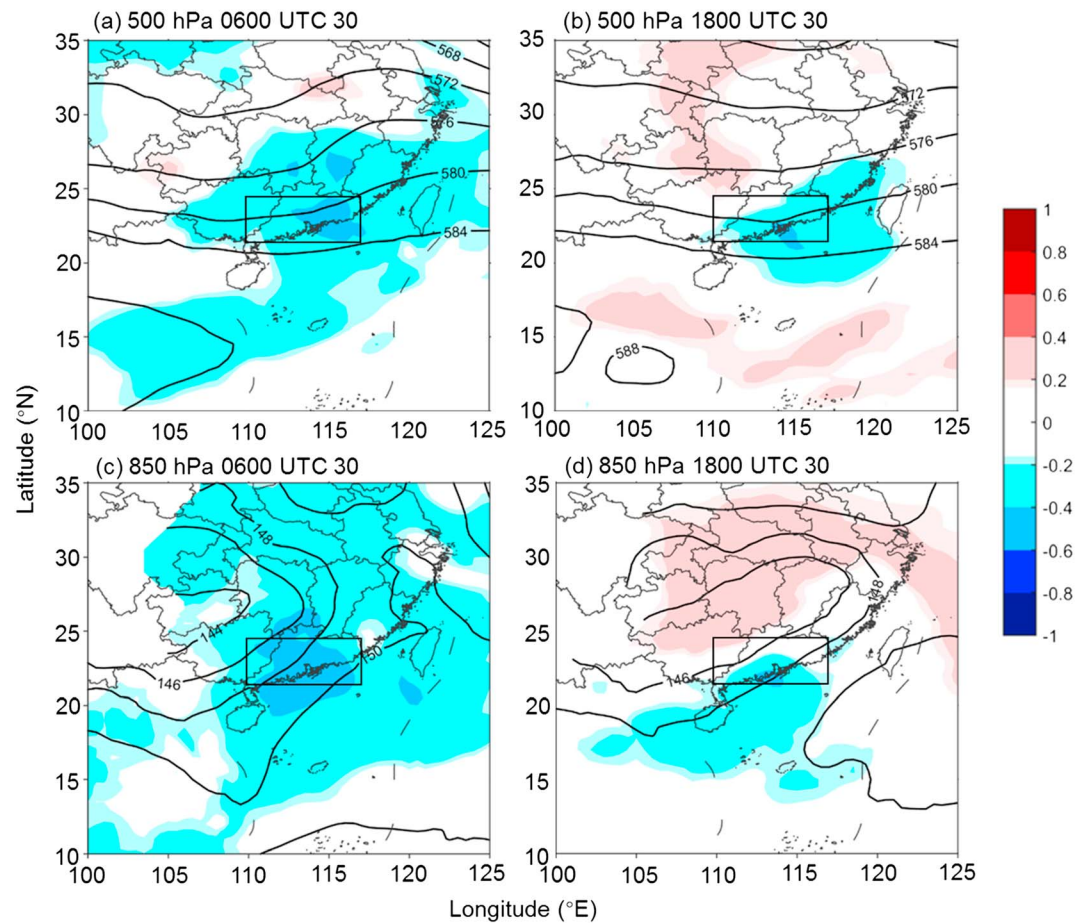


Figure 9. Correlation coefficient (shading) between area-averaged accumulated precipitation in S1 and (a) 500-hPa and (c) 850-hPa geopotential height at 0600 UTC 30 March 2014. Values over 0.1602 are shaded, representing that the linear relationship in those areas is significant at the 95% confidence level (the same for the following correlation maps). The ensemble mean geopotential height at 0600 UTC 30 March 2014 is contoured in black every 40 gpm (20 gpm) on 500 hPa (850 hPa). (b) and (d) are as (a) and (c) but for correlation coefficient between the accumulated precipitation in S2 and the geopotential height at 1800 UTC 30 March 2014. The black boxes in all the panels denote the control area, the same as that in Figure 1.

vortex, Figure 11d), which was consistent with the correlation results. The reason could be that a weaker low-level vortex was associated with a narrower southerly flow, which was beneficial for heavy precipitation to focus over a smaller geographic area. Similar results were once obtained by Lynch and Schumacher (2014) in a rainfall case in the central U.S.

4.2.2. Low-Level Jet

Low-level jet can not only transport moisture but also determine the spatial distribution of surface rainfall. Previous studies have shown that a low-level jet is strongly correlated with heavy rainfall and associated MCSs (e.g., Chen et al., 2014, 2005; Nicolini et al., 1993; Squitieri & Gallus, 2016a, 2016b). As mentioned in section 3, during this persistent heavy rainfall, there was a strong southwesterly low-level jet along the southeast flank of the low-level vortex. The role of the low-level jet is examined in this section by calculating the correlations between 850-hPa wind speed and the accumulated precipitation of the two stages in a way similar to the geopotential height.

The 850-hPa wind speed in southeastern Guangdong and SCS at 0600 UTC 30 March was positively correlated with accumulated precipitation in S1 (Figure 12a). The positive signal was so strong that in Pearl River Delta region the correlation coefficient was over 0.6, far beyond that of significance level (0.1602). The maximum correlation coefficient was 0.6582, which was the largest magnitude among the correlations of both wind speed and geopotential height at all pressure levels with precipitation in both stages. This

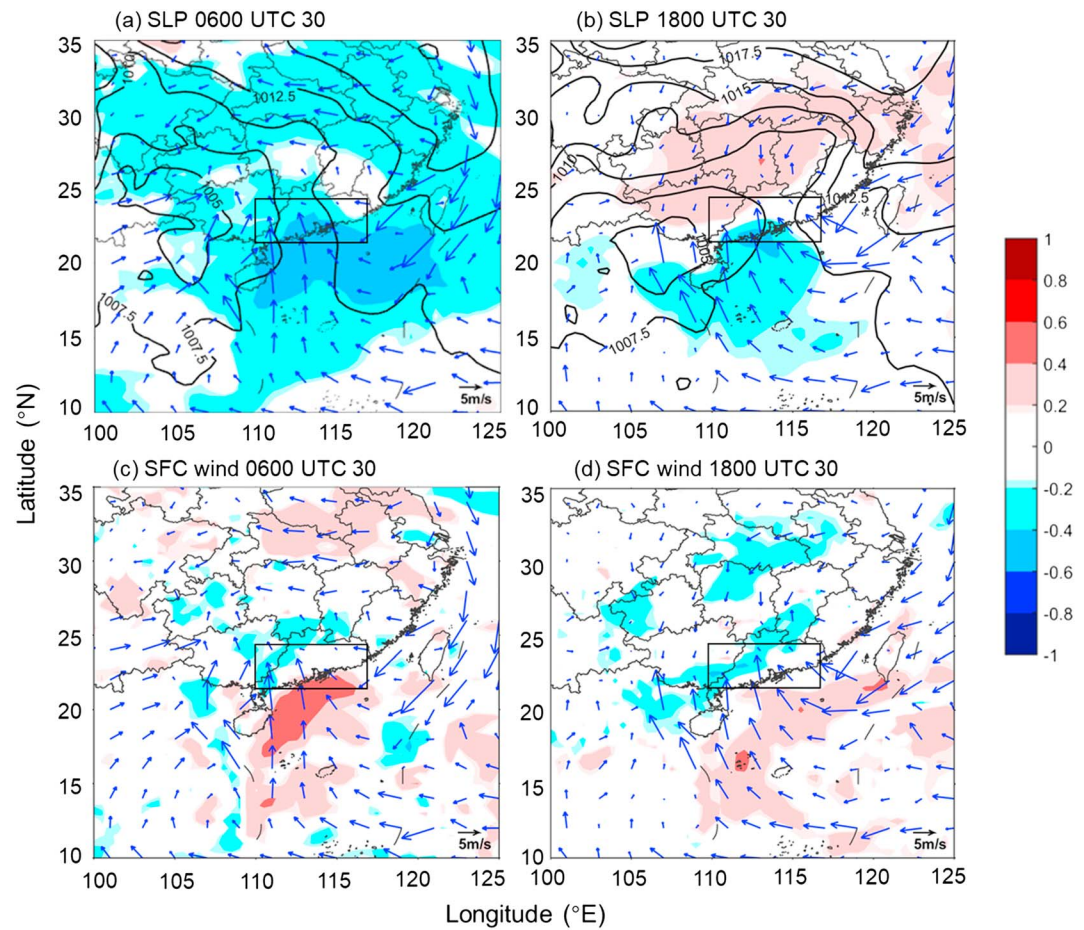


Figure 10. (a) Correlation coefficient (shading) between the accumulated precipitation in S1 and sea level pressure at 0600 UTC 30 March 2104. Also shown are the ensemble mean 10-m wind (blue vectors) and sea level pressure (black contour every 2.5 hPa) at this time. (b) is as (a) but for the correlation coefficient between the accumulated precipitation in S2 and sea level pressure at 1800 UTC 30 March, with the ensemble mean 10-m wind vector and sea level pressure contour at the corresponding time. (c) Correlation coefficient (shading) between the accumulated precipitation in S1 and 10-m wind speed at 0600 UTC 30 March. (d) is as (c) but for the correlation coefficient between the accumulated precipitation in S2 and 10-m wind speed at 1800 UTC 30 March. The wind vectors in (c) and (d) are the same as (a) and (b), respectively. The reference vectors are given at the bottom right. The black boxes in all the panels denote the control area, the same as that in Figure 1.

reinforced that in S1 a stronger low-level jet orienting from SCS to the southeast Guangdong was beneficial for heavy precipitation to occur. A comparison of 850-hPa wind speed between good and bad members in S1 at 0600 UTC 30 March (Figure 12c) was also consistent with the ESA results: The jet location in the composite of good members was more to the southeast than in the composite of bad members. These results demonstrate that when the low-level vortex was more to the southeast, the low-level jet generated from the high geopotential height gradient area was also more to the southeast and eventually led to the rainfall more to the southeast (e.g., Figures 8a and 8c).

In S2, there was a strong negative signal over the northwest flank of the jet region and a weak positive signal over the southeast flank of the jet region (Figure 12b), implying that a more-to-the-south northern boundary of the low-level jet would produce more rainfall in the control area. This was further confirmed by a comparison on wind speed between the good and bad members (Figure 12d). This result suggests that for heavy rainfall to occur in the control area in S2, the low-level jet should be narrower and not extend northwestward to central Guangxi and south Hunan (denoted in Figure 1), which was corroborated by the weaker low-level vortex in good members of S2 (Figure 11d).

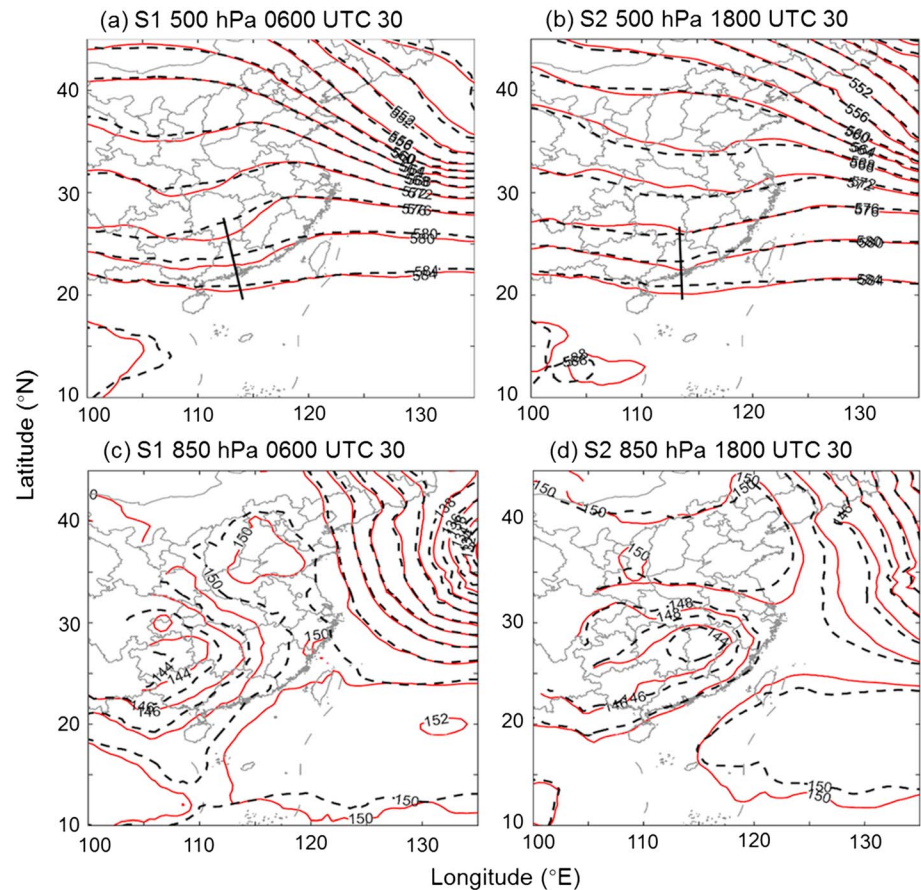


Figure 11. Comparisons between good member and bad member on composite 500-hPa and 700-hPa geopotential height. (a) Mean 500-hPa geopotential height of good (bad) members in S1 at 0600 UTC 30 March 2014 is contoured in red thin (black dash) every 40 gpm. The black thick line denotes the location of the short wave trough in the good member composite. (b) is as (a) but for typical members in S2 at 1800 UTC 30 March 2014. (c) Mean 850-hPa geopotential height of good (bad) members in S1 at 0600 UTC 30 March 2014 is contoured in red thin (black dash) every 20 gpm. (d) is as (c) but for typical members in S2 at 1800 UTC 30 March 2014.

Strong onshore winds were found near the surface (Figures 10c and 10d) associated with the 850-hPa jet, which was consistent with Chen et al. (2014). Surface onshore winds were also significantly correlated with the rainfall in a similar pattern as that for 850-hPa wind speed (Figures 10c and 10d), but with a smaller magnitude in both stages. Stronger surface onshore winds perpendicular to the southeast coast of Guangdong were likely to induce more intense rainfall.

Although land–sea breeze could be an essential mechanism that controls the diurnal variation of coastal rainfall in south China (Chen et al., 2015, 2016), the precipitation over the two stages in this event was probably not dominated by land–sea breeze. The land–sea breeze and associated diurnal cycle of precipitation were relatively weak (not shown) due to high southerly wind (Chen et al., 2017; Wang & Sobel, 2017). In addition, the spatial resolution of the ECMWF global ensemble forecast (~32 km) might be too coarse to resolve the precipitation associated with localized land–sea circulation.

4.2.3. Moisture

Correlations of total column water and moisture flux at different levels in the two stages were also calculated to diagnose the sensitivity of precipitation to moisture. In the correlation distribution of total column water in S1 (Figure 13a), there was a large positive area over Guangdong and SCS with a north–south orientation and a maximum magnitude greater than 0.4 and a weak negative area in Guizhou Province (denoted in Figure 1). This indicates that when the moisture from SCS was more sufficient, there would be more precipitation in the control area. As shown in the comparison on total column water between good and bad members at 0600 UTC 30 March (Figures 14a and 14b), both good and bad members forecasted a high moisture tongue

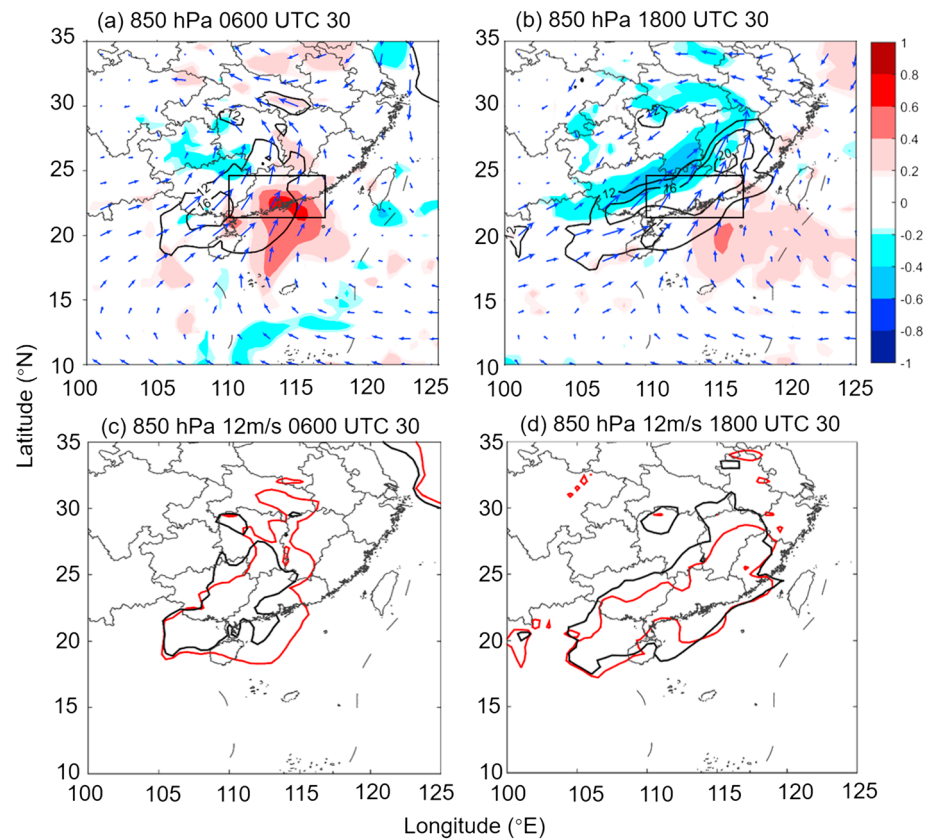


Figure 12. (a) Correlation coefficient (shading) between the accumulated precipitation in S1 and 850-hPa wind speed at 0600 UTC 30 March 2014. Also shown are the ensemble mean 850-hPa wind at this time (blue vectors) and the wind speed of >12 m/s (black contour) every 4 m/s. (b) is as (a) but for the correlation coefficient between the accumulated precipitation in S2 and 850-hPa wind speed at 1800 UTC 30 March, with the ensemble mean wind at the corresponding time. (c) The composite 850-hPa wind speed of 12 m/s at 0600 UTC 30 March in good (bad) members in S1 is contoured in red (black). (d) is as (c) but for the typical members in S2 at 1800 UTC 30 March. The black boxes in all the panels denote the control area, the same as that in Figure 1.

from SCS to Guangdong. However, in good members, the total column water maxima (over 50 mm) was located in central Guangdong (Figure 14a), while in bad members the maxima was approximately 5 mm smaller with more moisture extending to Guangxi (Figure 14b). Notably, the positive area of total column water (Figure 13a) was collocated with the 850-hPa wind speed positive signal in S1 (Figure 12a). A more-to-the-southeast low-level jet coupled with the high moisture tongue would lead to more precipitation (Figure 14c) in the control area. On the contrary, when the low-level jet was more to the northwest and was located outside the high moisture tongue (Figure 14b), it would transport less moisture to the northwest of Guangdong, leading to rainfall more to the northwest with a smaller precipitation amount compared with good members (Figure 14d).

In S2, the strong and extensive positive area oriented west–east over Guangdong and Guangxi with a small and weak negative area covering Hunan, northwest to Guangdong (Figure 13b). This suggests that increasing precipitation in S2 was closely related with more moisture over Guangxi and Guangdong. In good members (Figure 15a), at 1800 UTC 30 March, the moisture in central Guangdong and Guangxi was sufficient (over 50 mm), while in bad members (Figure 15b) the moisture was more to the north of the control area. Bad members forecasted a broader low-level jet, and thus high value of total column water, would be transported to south Hunan and Jiangxi (Figure 15b; these two provinces are denoted in Figure 1), which consequently resulted in less precipitation in the control area (Figure 15d). In contrast, a narrower low-level jet was more favorable for moisture to concentrate over Guangdong (Figure 15a) and eventually resulted in heavy rainfall (Figure 15c).

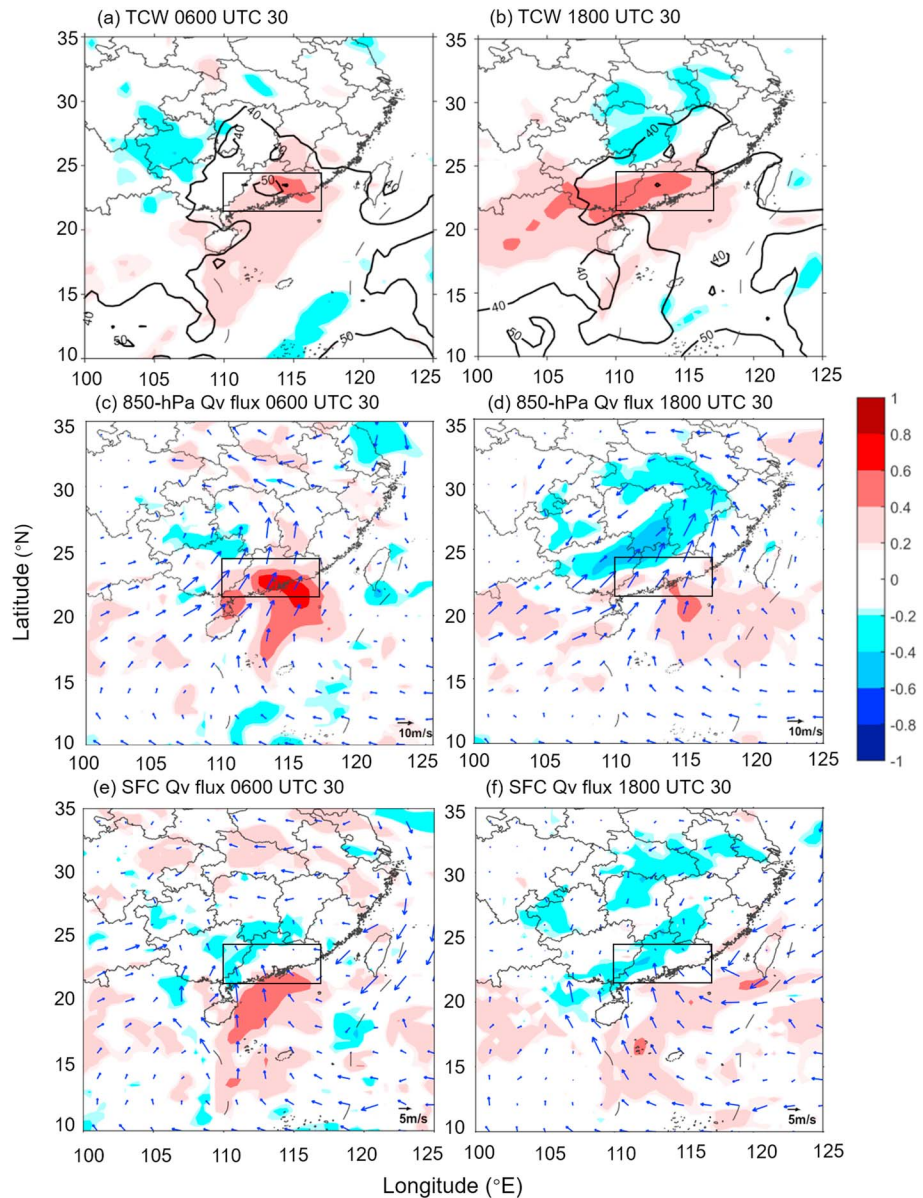


Figure 13. (a) Correlation coefficient (shading) between the area-averaged accumulated precipitation in S1 and the total column water at 0600 UTC 30 March 2014. The ensemble mean total column water (>40 mm) at 0600 UTC 30 March is contoured in black every 10 mm. (b) is as (a) but for the correlation coefficient between the accumulated precipitation in S2 and the total column water at 1800 UTC 30 March. Correlation coefficient (shading) between the area-averaged accumulated precipitation in S1 and the magnitude of 850-hPa water vapor flux at 0600 UTC 30 March is given in (c). The ensemble mean 850-hPa wind vector at 0600 UTC 30 March is also shown (blue vectors). (d) is as (c) but for the correlation coefficient between the accumulated precipitation in S2 and the magnitude of 850-hPa water vapor flux at 1800 UTC 30 March and 850-hPa wind vector at corresponding time. (e) and (f) are as (c) and (d) but for correlations between surface water vapor flux and precipitation and the ensemble mean surface wind (blue vectors). The black boxes in all the panels denote the control area, the same as that in Figure 1. The reference vectors are given at the bottom right.

The above results were reconfirmed by the correlation distribution of water vapor flux at different levels (Figures 13c–13f). Similar correlation patterns were found at different levels with the maximum magnitude at 850 hPa. The correlation distribution of water vapor flux at 850 hPa (Figures 13c and 13d) greatly resembled that of 850-hPa wind speed (Figures 12a and 12b), which implies that characteristics of low-

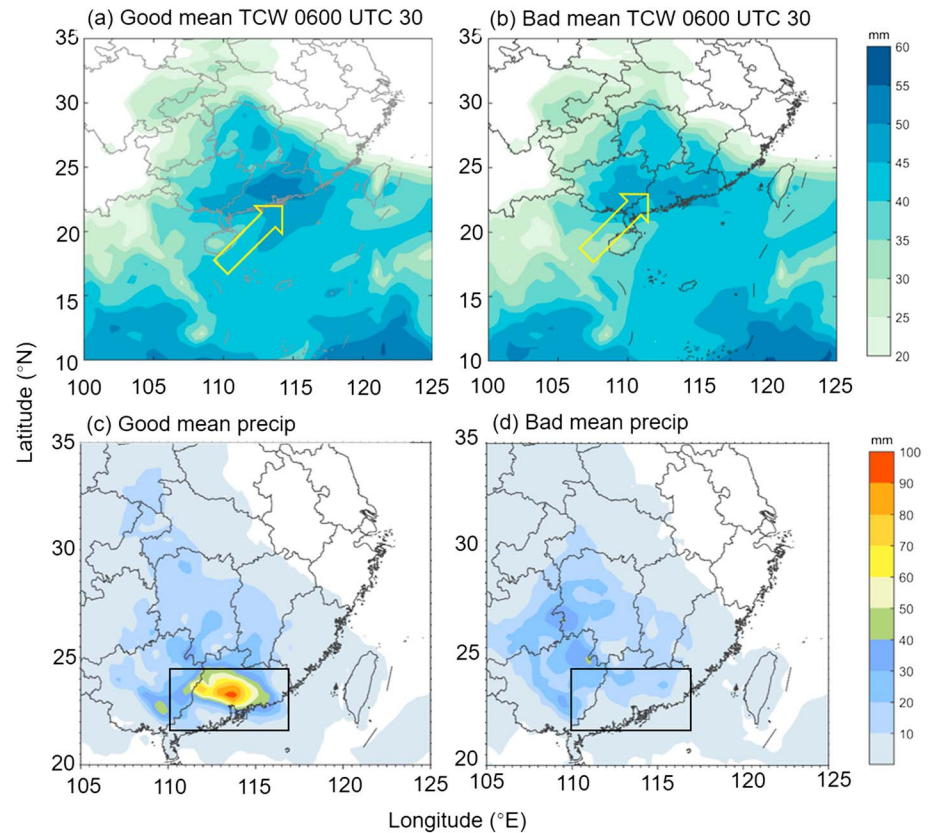


Figure 14. Composite total column water (over 20 mm) of good members and bad members in S1 at 0600 UTC 30 March 2014 are shaded in (a) and (b), respectively. The yellow arrow is a conceptual representation of 850-hPa low-level jet at corresponding time. Good member and bad member mean accumulated precipitation in S1 are plotted in (c) and (d), respectively. The black boxes in (c) and (d) denote the control area, the same as that in Figure 1.

level jet dominantly influenced the low-level horizontal moisture transport. In S1, there was a significant positive signal in southeastern Guangdong and SCS, which suggests that stronger low-level moisture transport would lead to a larger precipitation amount (Figure 13c). In S2, the stronger low-level moisture transport near the southeast flank of the jet region associated with a broader low-level jet was detrimental for rainfall accumulation in the control area (Figure 13d). Although not as strong as that of 850-hPa moisture transport, the correlation between surface water vapor flux and precipitation was still significant (Figures 13e and 13f). More surface moisture transport along the southeast coast of Guangdong associated with stronger surface onshore wind (Figures 10c and 10d) was favorable for heavy rainfall in the control area.

Results in section 4.2 show that the low-level jet played an essential role in both stages but influenced the precipitation in different ways. In S1, the location of the low-level jet influenced the precipitation amount significantly. A low-level jet more to the southeast was beneficial for more precipitation in the control area. In S2, however, it was the width of the low-level jet that made the difference: a broader low-level jet was detrimental for heavy rainfall to occur in the control area because it would transport more water vapor to the northern places.

4.3. Reasons for Different Forecast Skills of the Rainfall in the Two Stages

Previous ESA results pinpointed the different favorable and detrimental conditions for the heavy rainfall in the two stages and revealed that the low-level jet played an essential role during this rainfall process. This section further analyzes the low-level wind ensemble forecast to understand the different rainfall forecast skills in the two stages.

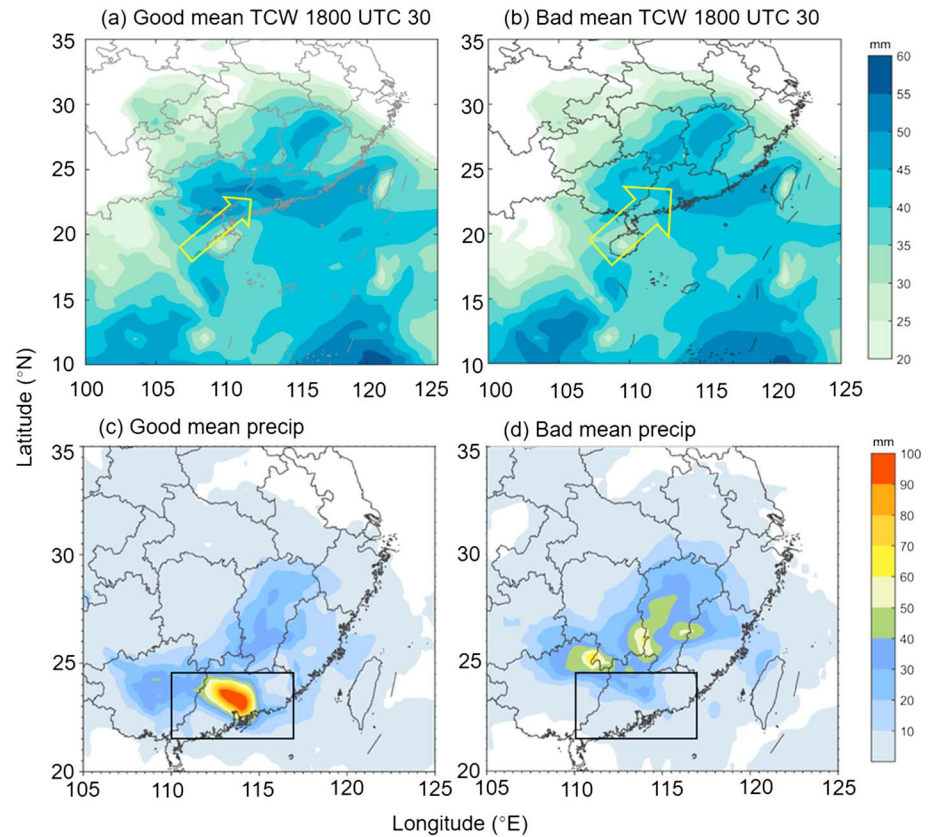


Figure 15. As in Figure 14 but for S2 at 1800 UTC 30 March 2014.

Results show that the spread of the low-level jet axis had different features in the two stages. The 850-hPa jet axis of the 150 ensemble members at 0600 and 1800 UTC 30 March were objectively identified (The MATLAB function “regionprops” was applied to determine the jet axis based on the center, length, and orientation of the major axis of the ellipse that has the same normalized second central moments as the large wind speed region (850-hPa wind speed over 15 m/s). More information about this function can be found in <https://www.>

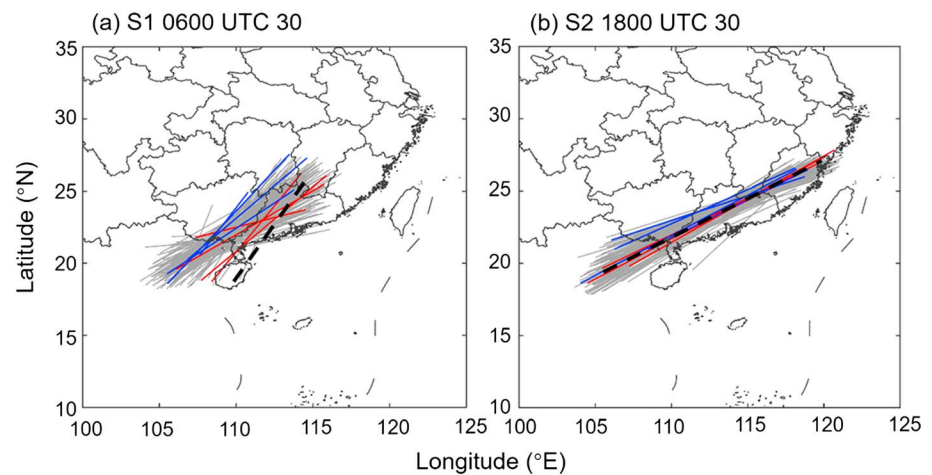


Figure 16. The 850-hPa jet axis of the 150 members (grey) at (a) 0600 and (b) 1800 UTC 30 March 2014. Good (bad) members of S1 are plotted in red (blue) in (a). Good (bad) members of S2 are plotted in red (blue) in (b). The black dashed thick line indicates the location of the jet axis of ERA-Interim reanalysis at corresponding time. The jet axis was identified automatically using MATLAB inner function regionprops based on the area where 850-hPa wind speed is over 15 m/s.

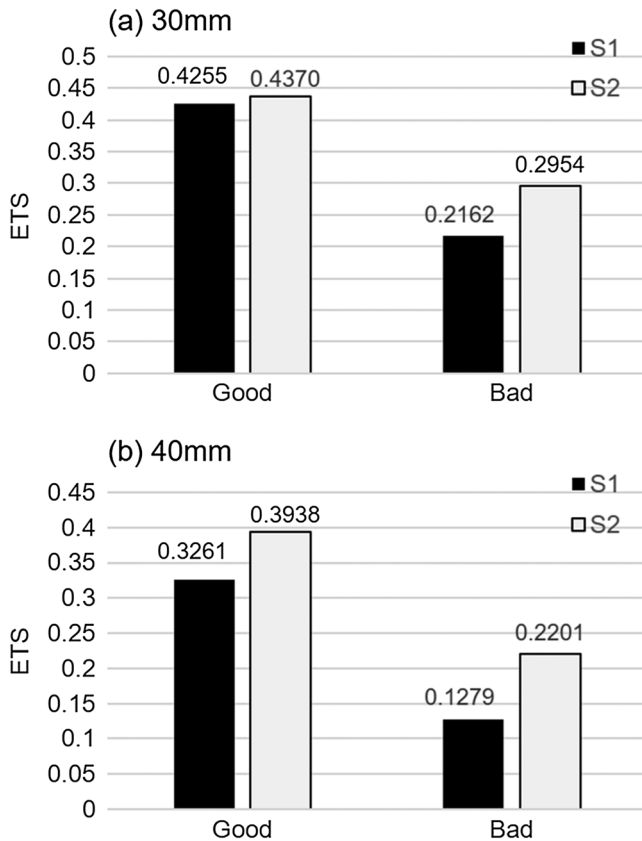


Figure 17. Mean ETS for thresholds of (a) 30 and (b) 40 mm of good subset (top 50%) and bad subset (bottom 50%) in the two stages (black bar for S1 and gray bar for S2).

mathworks.com/help/images/ref/regionprops.html?s_tid=gn_loc_drop.) based on the morphology of the area with wind speed beyond 15 m/s (Figure 16). In S1, the distribution of jet axis was more widespread than that in S2, indicating that the location of the low-level jet at this time was quite diverse and difficult to predict accurately. In general, the positions of jet axis in bad members (blue lines in Figure 16a) were more to the northwest and good members more to the southeast (red lines in Figure 16a), which was consistent with the previous ESA results on low-level jet. The jet axis from the ERA reanalysis (the dashed black line in Figure 16a) was located to the southeast of most ensemble members, and this explained why the ensemble rainfall forecast was more to the northwest with less precipitation amount compared with observation (Figures 6a and 6b). In S2 (Figure 16b), the jet axis location spread was much smaller, concentrating around the jet axis of ERA reanalysis. The difference in the jet axis locations between good and bad members in S2 was not as obvious as that in S1.

These results suggest that an accurate jet location played a major role in the higher skill of rainfall forecast in the control area. When the jet location was accurate, even though the jet was forecasted slightly broader, it might not decrease the precipitation in the control area as significantly as the jet location bias in S1. This was confirmed by the worse rainfall forecast skill of bad members in S1 than bad members in S2. For each stage, the 150-member ensemble was divided into good subset and bad subset according to ETS. The good subset included members whose ETS was larger than median (top 50%), and the bad subset includes members whose ETS was lower than median (bottom 50%).

Figure 17 shows that the forecast skills in S1 were worse than those in S2 in both good and bad subsets for different thresholds. However, the difference between S1 and S2 in the bad subset was apparently larger than that in the good subset. This implies that a worse subset in S1 might contribute to the lower ensemble mean forecast skill on precipitation in this stage.

Figure 16 also indicates that the location of low-level jet axis in S1 was more sensitive to small perturbations in initial conditions, while the location of low-level jet in S2 was less widespread, and thus was easier for the ensemble forecast to capture. The spread of the jet axis location was found to be greatly dependent on the direction of vortex movement and the orientation of the low-level jet. As previously described, the location of the low-level jet was associated with the geopotential height in the neighborhood. The forecast uncertainty in the geopotential height in Guangdong partly resulted from the uncertainty of the low-level vortex. The track of the low-level vortex during this heavy rainfall case (Figure 18) showed different directions of the vortex movement in the two stages: the low-level vortex moved to the southeast from 0000 to 1200 UTC 30 March (S1) and then to the northeast from 1200 UTC 30 March to 0000 UTC 31 March (S2). Consequently, the direction of vortex movement in S1 was nearly perpendicular to the low-level jet, while in S2 the direction of vortex movement was more parallel to the low-level jet. When the vortex motion was perpendicular to the low-level jet (S1), the uncertainty of the location of low-level vortex could significantly change the uncertainty of geopotential height in the control area. As a result, there would be a larger uncertainty in the location of the low-level jet. On the contrary, when the vortex motion was approximately parallel to the low-level jet, the magnitude of geopotential height in the control area was more stable even with the changing vortex location within the ensemble. This was corroborated by the evolution of 850-hPa geopotential height ensemble spread in the control area (Figure 19). Generally, the ensemble spread of geopotential height tended to increase with time continuously. However, all the three ensembles initiated at three different times presented a local maximum of geopotential height spread over the control area at around 0600 UTC 30 March, indicating the larger geopotential height uncertainty when the vortex moved southeastward than that when the vortex moved northeastward. Therefore, the changing low-level system motion direction in different stages influenced the uncertainty of jet axis location through geopotential height in the control area.

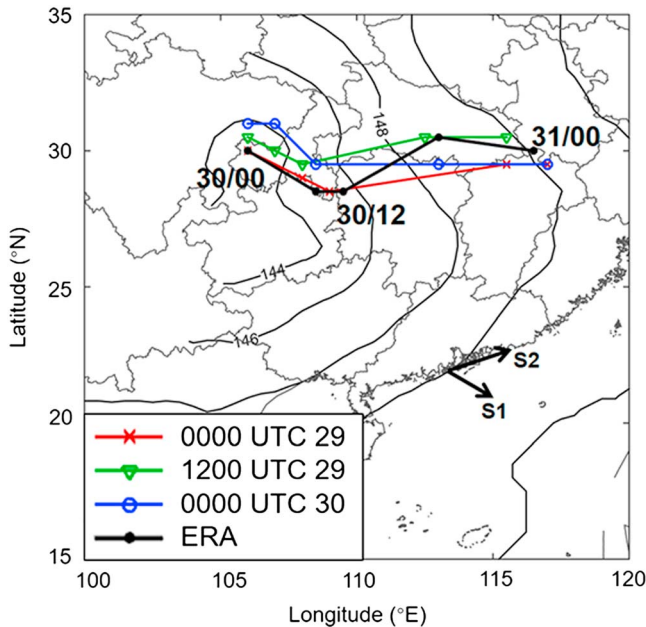


Figure 18. Track of low-level vortices in the ERA analysis and different ensemble forecasts. The centers of the 700-hPa low-level vortex (minimum of geopotential height) in the ensemble mean that initialized at 0000 UTC 29 March (red cross), 1200 UTC 29 March (green triangle), 0000 UTC 30 March 2014 (blue circle), and ERA-Interim (black dots) are marked every 6 hr from 0000 UTC 30 March to 0000 UTC 31 March. The 700-hPa height field can not only effectively reflect the movement of low-level vortex but also avoid the topographic effects on lower pressure level. The 850-hPa geopotential height at 0000 UTC 30 March is contoured in black every 20 gpm, representing the low-level synoptic circulation during this event. The thick black arrows in southeast Guangdong represent the direction of the movement of the low-level vortex in S1 and S2.

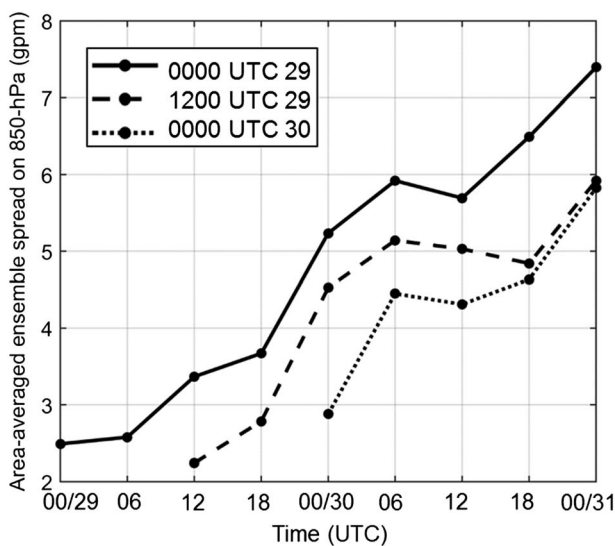


Figure 19. Evolution of area-averaged ensemble spread of 850-hPa geopotential height over the black box in Figure 1. The solid, dashed, and dotted lines indicate the ensemble forecast initialized at 0000 UTC 29 March, 1200 UTC 29 March, and 0000 UTC 30 March, respectively.

5. Summary and Conclusions

In this study, the stage-dependent rainfall forecast skill in a persistent heavy rainfall in south China and the underlying synoptic-scale features were investigated using global ensemble forecast from ECMWF. During 29–31 March 2014, two rainfall stages were clearly identified in Guangdong from rain gauge observation. The ensemble forecast of ECMWF had a higher forecast skill of precipitation in the second stage (S2) than the first stage (S1), presenting a stage-dependent feature.

By applying ensemble-based sensitivity analysis (ESA), different key synoptic-scale factors that influenced the rainfall forecast uncertainty of the two stages were diagnosed by correlating accumulated precipitation to atmospheric state variables for each stage respectively. Results showed that the precipitation in both stages was positively correlated with the strength of midlevel short trough and sensitive to the position and strength of the low-level vortex and the low-level jet on the southeast flank of the vortex.

The low-level jet (and its associated moisture transport) was most essential among these significant synoptic-scale impact factors in this heavy rainfall event due to its strongest linear correlation with rainfall. The low-level jet influenced the precipitation in S1 and S2 in different ways. In S1, the rainfall forecast uncertainty was mainly from the location of the low-level jet. When the low-level vortex was more to the southeast, the low-level jet generated from the tight pressure gradient would also move more to the southeast, contributing to a better rainfall forecast in Guangdong and its coastal area. In S2, however, the rainfall forecast uncertainty mainly came from the width of the low-level jet. A weaker low-level vortex was associated with a narrower low-level jet, which led to the transport of moisture focusing in the control area and resulted in a better rainfall forecast in Guangdong.

The stage-dependent forecast skills of precipitation in this case could be attributed to the different forecast uncertainties of the low-level jet location in the two stages, which might be relevant to the specific atmospheric flow pattern and the direction of system movement. The lower forecast skill of precipitation in S1 was strongly associated with the less accurate location of the low-level jet in the ensemble forecast. Examinations on the jet axis of the ensemble forecast showed that locations of low-level jet axis in S1 were diverse among ensemble members, while in S2 they were more concentrated and better captured by the model. When the low-level vortex was moving southeastward (perpendicular to the low-level jet), the geopotential height uncertainty in the control area was large, conducive to a wide ensemble spread of the jet location in S1. After that the low-level vortex moved northeastward (parallel to the low-level jet), leading to a smaller height uncertainty in the control area and thus the jet locations were more concentrated and well predicted in S2. Once the jet location was correctly forecasted (as in S2), even though the jet width was forecasted slightly broader, it would not decrease the precipitation in the control area as significantly as the jet location bias (as in S1).

This study suggests that the uncertainty of low-level jet in operational numerical model can exert prominent influence on quantitative forecast skills of heavy rainfall in south China. The forecast uncertainty of the low-level jet location in different rainfall stages can be strongly

influenced by the juxtaposition between the low-level system motion and the low-level jet. The variability of this juxtaposition is probably the primary cause of the stage-dependent precipitation forecast skills, which even overweighs the influence of forecast lead time. Such a variation in the juxtaposition of the low-level vortex and the low-level jet has been also observed in other heavy rainfall processes in south China (e.g., Fu et al., 2010; Huang & Meng, 2014).

Acknowledgments

This work was supported by the National Natural Science Foundation of China (grants 41461164006, 41425018, and 41375048) and Ministry of Science and Technology of the People's Republic of China grant GYHY201306004. Rainfall observations and radar imageries were provided by the National Meteorological Information Center of China Meteorological Administration (<http://www.cma.gov.cn/2011qxw/2011qsjgx/>). The ERA-Interim was downloaded from <http://apps.ecmwf.int/datasets/data/interim-full-daily/levtype=sfc/>. The ECMWF global ensemble forecast was downloaded from <http://apps.ecmwf.int/datasets/data/tigge/levtype=sfc/type=pf/>. All authors of this manuscript do not have a conflict of interest to declare.

References

- Ancell, B. C. (2013). Nonlinear characteristics of ensemble perturbation evolution and their application to forecasting high-impact events. *Weather Forecasting*, 28, 1353–1365. <https://doi.org/10.1175/WAF-D-12-00090.1>
- Bednarczyk, C. N., & Ancell, B. C. (2015). Ensemble sensitivity analysis applied to a southern plains convective event. *Monthly Weather Review*, 143(1), 230–249. <https://doi.org/10.1175/MWR-D-13-00321.1>
- Bougeault, P., Toth, Z., Bishop, C., Brown, B., Burridge, D., Chen, D. H., et al. (2010). The THORPEX interactive grand global ensemble. *Bulletin of the American Meteorological Society*, 91(8), 1059–1072. <https://doi.org/10.1175/2010BAMS2853.1>
- Chen, G. T.-J. (1983). Observational aspects of the Mei-Yu phenomena in subtropical China. *Journal of the Meteorological Society of Japan*, 61(2), 306–312. https://doi.org/10.2151/jmsj1965.61.2_306
- Chen, W., Chen, G., & Lin, D. (2005). Characteristics of low-level jets over northern Taiwan in Mei-Yu season and their relationship to heavy rain events. *Monthly Weather Review*, 133, 20–43.
- Chen, X., Zhang, F., & Zhao, K. (2016). Diurnal variations of the land-sea breeze and its related precipitation over South China. *Journal of the Atmospheric Sciences*, 73(12), 4793–4815. <https://doi.org/10.1175/JAS-D-16-0106.1>
- Chen, X., Zhang, F., & Zhao, K. (2017). Influence of monsoonal wind speed and moisture content on intensity and diurnal variations of the Mei-Yu season coastal rainfall over South China. *Journal of the Atmospheric Sciences*, 74(9), 2835–2856. <https://doi.org/10.1175/JAS-D-17-0081.1>
- Chen, X., Zhao, K., & Xue, M. (2014). Spatial and temporal characteristics of warm season convection over Pearl River Delta region, China, based on 3 years of operational radar data. *Journal of Geophysical Research: Atmospheres*, 119, 12,447–12,465. <https://doi.org/10.1002/2014JD021965>
- Chen, X., Zhao, K., Xue, M., Zhou, B., Huang, X., & Xu, W. (2015). Radar-observed diurnal cycle and propagation of convection over the Pearl River Delta during Mei-Yu season. *Journal of Geophysical Research: Atmospheres*, 120, 12,557–12,575. <https://doi.org/10.1002/2015JD023872>
- Cressman, G. P. (1959). An operational objective analysis system. *Monthly Weather Review*, 87(10), 367–374. [https://doi.org/10.1175/1520-0493\(1959\)087%3C0367:AOAS%3E2.0.CO;2](https://doi.org/10.1175/1520-0493(1959)087%3C0367:AOAS%3E2.0.CO;2)
- Davis, C., & Lee, W. (2012). Mesoscale analysis of heavy rainfall episodes from SoWMEX/TiMREX. *Journal of the Atmospheric Sciences*, 69(2), 521–537. <https://doi.org/10.1175/JAS-D-11-0120.1>
- Dee, D. P., Uppala, S. M., Simmons, A. J., Berrisford, P., Poli, P., Kobayashi, S., et al. (2011). The ERA-Interim reanalysis: Configuration and performance of the data assimilation system. *Quarterly Journal of the Royal Meteorological Society*, 137(656), 553–597. <https://doi.org/10.1002/qj.828>
- Feng, Y. H., Li, S., & Wen, D. Q. (2014). A historically rare incidence of extensive flight delays at Baiyun Airport on March 30–31, 2014, and analysis of characteristics of the associated process of severe convection. *Guangdong Meteorology*, 36(4), 6–10.
- Fu, S., Zhao, S., Sun, J., & Li, W. (2010). One kind of vortex causing heavy rainfall during pre-rainy season in South China (in Chinese). *Chinese Journal of Atmospheric Sciences*, 34(2), 235–252.
- Gao, S., Meng, Z., Zhang, F., & Bosart, L. (2009). observational analysis of heavy rainfall mechanisms associated with severe Tropical Storm Bills (2006) after its landfall. *Monthly Weather Review*, 137(6), 1881–1897. <https://doi.org/10.1175/2008MWR2669.1>
- Garcies, L., & Homar, V. (2009). Ensemble sensitivities of the real atmosphere: Application to Mediterranean intense cyclones. *Tellus*, 61A, 394–406.
- Hakim, G. J., & Torn, R. D. (2008). *Ensemble synoptic analysis. Synoptic–dynamic meteorology and weather analysis and forecasting: A tribute to Fred Sanders, Meteor. Monogr.*, No. 55 (pp. 147–161). Boston, MA: Amer. Meteor. Soc.
- Hawblitzel, D. P., Zhang, F., Meng, Z., & Davis, C. A. (2007). Probabilistic evaluation of the dynamics and predictability of the mesoscale convective vortex of 10–13 June 2003. *Monthly Weather Review*, 135(4), 1544–1563. <https://doi.org/10.1175/MWR3346.1>
- Huang, L., & Meng, Z. (2014). Quality of the target area for metrics with different nonlinearities in a mesoscale convective system. *Monthly Weather Review*, 142(7), 2379–2397. <https://doi.org/10.1175/MWR-D-13-00244.1>
- Kuo, Y., & Chen, G. (1990). The Taiwan Area Mesoscale Experiment (TAMEX): An overview. *Bulletin of the American Meteorological Society*, 71(4), 488–503. [https://doi.org/10.1175/1520-0477\(1990\)071%3C0488:TTAMEA%3E2.0.CO;2](https://doi.org/10.1175/1520-0477(1990)071%3C0488:TTAMEA%3E2.0.CO;2)
- Le Dimet, F., & Talagrand, O. (1986). Variational algorithms for analysis and assimilation of meteorological observations: Theoretical aspects. *Tellus*, 38A(2), 97–110. <https://doi.org/10.1111/j.1600-0870.1986.tb00459.x>
- Li, J., Chen, Y., & Lee, W. (1997). Analysis of a heavy rainfall event during TAMEX. *Monthly Weather Review*, 125(6), 1060–1082. [https://doi.org/10.1175/1520-0493\(1997\)125%3C1060:AOAHRE%3E2.0.CO;2](https://doi.org/10.1175/1520-0493(1997)125%3C1060:AOAHRE%3E2.0.CO;2)
- Luo, Y., Zhang, R., Wan, Q., Wang, B., Wong, W. K., Hu, Z., et al. (2017). The Southern China Monsoon Rainfall Experiment (SCMREX). *Bulletin of the American Meteorological Society*, 98(5), 999–1013. <https://doi.org/10.1175/BAMS-D-15-00235.1>
- Lynch, S., & Schumacher, R. (2014). Ensemble-based analysis of the May 2010 extreme rainfall in Tennessee and Kentucky. *Monthly Weather Review*, 142(1), 222–239. <https://doi.org/10.1175/MWR-D-13-00020.1>
- McMurdie, L. A., & Ancell, B. (2014). Predictability characteristics of land-falling cyclones along the North American west coast. *Monthly Weather Review*, 142(1), 301–319. <https://doi.org/10.1175/MWR-D-13-00141.1>
- Mu, M., & Duan, W. (2003). A new approach to studying ENSO predictability: Conditional nonlinear optimal perturbation. *Chinese Science Bulletin*, 48, 1045–1047. <https://doi.org/10.1007/BF03184224>
- Nicolini, M., Waldron, K., & Paegle, J. (1993). Diurnal oscillations of low-level jets, vertical motion, and precipitation: A model case study. *Monthly Weather Review*, 121(9), 2588–2610. [https://doi.org/10.1175/1520-0493\(1993\)121%3C2588:DOOLL%3E2.0.CO;2](https://doi.org/10.1175/1520-0493(1993)121%3C2588:DOOLL%3E2.0.CO;2)
- Park, Y. Y., Buizza, R., & Leutbecher, M. (2008). TIGGE: Preliminary results on comparing and combining ensembles. *Quarterly Journal of the Royal Meteorological Society*, 134(637), 2029–2050. <https://doi.org/10.1002/qj.334>
- Schumacher, R. (2011). Ensemble-based analysis of factors leading to the development of a multiday warm-season heavy rain event. *Monthly Weather Review*, 139(9), 3016–3035. <https://doi.org/10.1175/MWR-D-10-05022.1>

- Sippel, J. A., & Zhang, F. (2008). A probabilistic analysis of the dynamics and predictability of tropical cyclogenesis. *Journal of the Atmospheric Sciences*, 65(11), 3440–3459. <https://doi.org/10.1175/2008JAS2597.1>
- Sippel, J. A., & Zhang, F. (2010). Factors affecting the predictability of Hurricane Humberto (2007). *Journal of the Atmospheric Sciences*, 67(6), 1759–1778. <https://doi.org/10.1175/2010JAS3172.1>
- Squitieri, B., & Gallus, W. (2016a). WRF forecasts of Great Plains nocturnal low-level jet-driven MCSs. Part I: Correlation between low-level jet forecast accuracy and MCS precipitation forecast skill. *Weather Forecasting*, 31(4), 1301–1323. <https://doi.org/10.1175/WAF-D-15-0151.1>
- Squitieri, B., & Gallus, W. (2016b). WRF forecasts of Great Plains nocturnal low-level jet-driven MCSs. Part II: Differences between strongly and weakly forced low-level jet environments. *Weather Forecasting*, 31(5), 1491–1510. <https://doi.org/10.1175/WAF-D-15-0150.1>
- Tao, S., & Ding, Y. (1981). Observational evidence of the influence of the Qinghai-Xizang (Tibet) Plateau on the occurrence of heavy rain and severe convective storms in China. *Bulletin of the American Meteorological Society*, 62(1), 23–30. [https://doi.org/10.1175/1520-0477\(1981\)062%3C0023:OEOTIO%3E2.0.CO;2](https://doi.org/10.1175/1520-0477(1981)062%3C0023:OEOTIO%3E2.0.CO;2)
- Torn, R. D. (2010). Diagnosis of the downstream ridging associated with extratropical transition using short-term ensemble forecasts. *Journal of the Atmospheric Sciences*, 67(3), 817–833. <https://doi.org/10.1175/2009JAS3093.1>
- Wang, C., Hsu, J. C.-S., Chen, G. T.-J., & Lee, D. (2014a). A study of two propagating heavy-rainfall episodes near Taiwan during SoWMEX/TIMREX IOP-8 in June 2008. Part I: Synoptic evolution, episode propagation, and model control simulation. *Monthly Weather Review*, 142(8), 2619–2643. <https://doi.org/10.1175/MWR-D-13-00331.1>
- Wang, C., Hsu, J. C.-S., Chen, G. T.-J., & Lee, D. (2014b). A study of two propagating heavy-rainfall episodes near Taiwan during SoWMEX/TIMREX IOP-8 in June 2008. Part II: Sensitivity tests on the roles of synoptic conditions and topographic effects. *Monthly Weather Review*, 142(8), 2644–2664. <https://doi.org/10.1175/MWR-D-13-00330.1>
- Wang, H., Luo, Y., & Jou, B. J.-D. (2014). Initiation, maintenance, and properties of convection in an extreme rainfall event during SCMREX: Observational analysis. *Journal of Geophysical Research: Atmospheres*, 119, 13, 206–13,232. <https://doi.org/10.1002/2014JD022339>
- Wang, S., & Sobel, A. H. (2017). Factors controlling rain on small tropical islands: Diurnal cycle, large-scale wind speed, and topography. *Journal of the Atmospheric Sciences*, 74(11), 3515–3532. <https://doi.org/10.1175/JAS-D-16-0344.1>
- Wang, X. F., & Cheng, Z. Q. (2014). *Analyses on the dynamical and thermal conditions of the successive and severe convection on the beginning of rainy season in Guangdong Province in 2014*. Paper presented at the 31th Annual Conference of Chinese Meteorological Society, Beijing, China.
- Wilks, D. S. (1995). *Statistical methods in the atmospheric sciences: An introduction* (p. 467). San Diego, CA: Academic Press.
- Wu, L., Huang, R., He, H., Shao, Y., & Wen, Z. (2010). Synoptic characteristics of heavy rainfall events in pre-monsoon season in South China. *Advances in Atmospheric Sciences*, 27(2), 315–327. <https://doi.org/10.1007/s00376-009-8219-z>
- Wu, M., & Luo, Y. (2016). Mesoscale observational analysis of lifting mechanism of a warm-sector convective system producing the maximal daily precipitation in China mainland during pre-summer rainy season of 2015. *Journal of Meteorological Research*, 30(5), 719–736. <https://doi.org/10.1007/s13351-016-6089-8>
- Yu, H., & Meng, Z. (2016). Key synoptic-scale features influencing the high-impact heavy rainfall in Beijing, China on 21 July 2012. *Tellus*, 68A, 31045.
- Yu, H., Wang, H., Meng, Z., Mu, M., Huang, X., & Zhang, X. (2017). A WRF-based tool for forecast sensitivity to the initial perturbation: The conditional nonlinear optimal perturbations versus the first singular vector method and comparison to MM5. *Journal of Atmospheric and Oceanic Technology*, 34(1), 187–206. <https://doi.org/10.1175/JTECH-D-15-0183.1>
- Zhang, R. H., Ni, Y. Q., Liu, L. P., Luo, Y., & Wang, Y. (2011). South China Heavy Rainfall Experiments (SChEREX). *Journal of the Meteorological Society of Japan*, 89A, 153–166. <https://doi.org/10.2151/jmsj.2011-A10>